ACS OMEGA

Article

Cite This: ACS Omega 2019, 4, 7200−7212

http://pubs.acs.org/journal/acsodf

Structures, Photoresponse Properties, and Biological Activity of Dicyano-Substituted 4-Aryl-2-pyridone Derivatives

Tripti Mandal,[†] Sudipta Pathak,[‖] Arka Dey,[‡,⊥] Md. Maidul Islam,[#] Saikat Kumar Seth,[‡] Abdulla Al Masum,[§] Joaquín Ortega-Castro,[▽] Partha Pratim Ray,[‡] Antonio Frontera,*[,▽] and Subrata Mukhopadhyay*[,†]

[†]Department of Chemistry, [‡]Department of Physics, and [§]Department of Life Science & Bio-technology, Jadavpur University, Kolkata 700032, India

[‖]Department of Chemistry, Haldia Government College, Debhog, Purba Medinipur, West Bengal 721657, India

[⊥]Department of Condensed Matter Physics and Material Sciences, S. N. Bose National Centre for Basic Sciences, Block JD, Sec. III, Salt Lake, Kolkata 700106, India

[#]Department of Chemistry, Aliah University, Action Area IIA/27, Kolkata 700156, India

[▽]Departament de Química, Universitat de les Illes Balears, Crta. de Valldemossa km 7.5, 07122 Palma de Mallorca, Baleares, Spain

Supporting Information

ABSTRACT: Described in this work is the synthesis of a novel dicyano-substituted *N*-2-aminoethyl-4-(3-pyridinyl)-2-pyridone organic compound (**1**) that is characterized by several spectroscopic methods. Compound (**1**) was utilized for the preparation of its perchlorate (**2**), chloride (**3**), and bromide (**4**) salts. Single-crystal X-ray structures of these three salts were determined, and noncovalent weak interactions involving the aromatic rings, anions, and water molecules in (**2**−**4**) were investigated in detail. Solid-state UV−vis spectrum of the reported compounds (**1**−**4**) was utilized to calculate their optical band gaps, which clearly indicated that they belong to the semiconductor family. Under illumination condition, the magnitudes of electrical properties of (**1**) and its salts (**2**−**4**) improve remarkably although the improvement differs from salt to salt and the result was analyzed theoretically. Salt (**2**) was tested for its DNA binding ability.

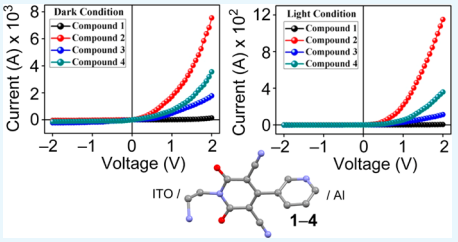

INTRODUCTION

Development of organic-based semiconducting materials has gained sufficient interest nowadays over the metal−organic semiconductors because of their facile manufacturing and processing, lower production cost, flexibility, light weight, and trouble-free way of deposition of films over a large surface.[1−6] These kind of semiconducting materials have applications in various technological fields and in optoelectronic devices, like photoconductors, sensors, organic light-emitting diodes, memory devices, organic field effect transistors, etc.[7−13] In spite of these advantages, the electrical transport property for organic semiconductors might be expected to be poor than that of the conventional inorganic semiconductors because of the absence of metals. However, salt formation of organic compounds introduces ionicity, which enhances relatively weak electrical transport properties of organic semiconductors[14−16] and salt forms can exhibit lower band gap than their base forms.[17,18] The design and synthesis of the solid-state supramolecular architecture of organic molecules through molecular self-assembly has experienced dynamic growth throughout the years.[19−24] From the view of noncovalent interactions, crystals of an organic compound are considered as the "ultimate supermolecule" because they are connected via relatively weak forces in comparison with interactions present in inorganic compounds.[20,25] Salt formation of these organic molecules through protonation can exclusively introduce a variety of additional noncovalent interactions as the counter ions formed during protonation can participate in noncovalent interactions like anion···π, anion···π^+, π···π^+, and π^+···π^+, which can give a new orientation to the existing structure.[26−30] Besides, in semiconducting materials, the extent and effectiveness of charge transport is governed by the relative orientation of components of participating molecules in a solid state.[31−35]

2-Pyridone core represents a diverse group of fascinating organic compounds having a broad spectrum of biological and pharmacological activities.[36−40] Some 2-pyridone derivatives can be prepared through very rapid and economic one-pot multicomponent coupling reactions.[41,42] Apart from this, the way of salt formation of these 2-pyridone derivatives is very elegant and getting the crystal form of salts is quite rapid.

In the present study, we have synthesized 1-(2-aminoethyl)-6-hydroxy-2-oxo-4-(3-pyridinyl)-1,2-dihydropyridine-3,5-dicarbonitriles (**1**) and three of its salts [perchlorate (**2**), chloride (**3**), and bromide (**4**)] (Figure 1). We have established the X-ray crystal structures of these salts and explored noncovalent

Received: January 31, 2019
Accepted: April 8, 2019
Published: April 22, 2019

DOI: 10.1021/acsomega.9b00289
ACS Omega 2019, 4, 7200−7212

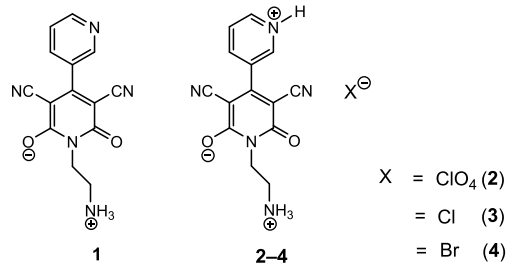

Figure 1. Structures of compounds (**1**–**4**).

interactions in their solid-state structure. We have also studied the electrical and photoresponse properties of (**1**) as well as its salts (**2**–**4**) to examine whether salts of this compound can improve the above-mentioned properties. The observed experimental band gaps (2–3 eV) indicate that they are wide-band gap semiconductors (WBGS)[43,44] and thus should have electronic properties in between those of typical semiconductors and insulators, allowing these materials to be potential candidates for operating at elevated temperatures, currents, and frequencies than traditional semiconductors.[45−47] WBGS materials are the key components used to fabricate LEDs and lasers, in some specific radio frequency function, specifically in military radars. Their intrinsic characteristics induce the potentiality for a broad area of application, and they are considered as the foremost contestants for the next-generation devices.[48−50] Moreover, considering the biological importance of our synthesized organic compounds, we have also explored the interaction of CT-DNA with one of the salts (**2**) in aqueous buffer medium.

RESULTS AND DISCUSSION

Crystallographic Analyses. Compounds (**2**–**4**) contain substituted 2-pyridone moiety with one protonated pyridine ring (ORTEP diagram and atom-numbering scheme of the cationic moiety is given in Supporting Information, Figure S1) along with different anions and solvent water molecules in their asymmetric units. Figure 2 represents the X-ray single-crystal structures of compounds (**2**–**4**) (crystal data and structure refinement parameters for (**2**–**4**) are provided (Table S1)). The protonated pyridine ring (C1–C5/N1) and the substituted 2-pyridone ring (C6–C10/N2) are designated as "ring A" and "ring B", respectively (Figure S1). Variation in the torsion angle between two aromatic rings and different orientations of the ethylammonium moiety (Figure 2) play a major role in differentiating solid-state structural arrangements as well as optical properties among the three salts.

The molecules of (**2**) are stabilized in the solid state through proper arrangement of hydrogen bonds, like N–H···O, C–H···O, and O–H···O along with lp···π, lp···π^+, anion···π, and anion···π^+ interactions (Tables S2 and S3). The protonated pyridine nitrogen is the H-bond donor to the water molecule that concurrently interacts with the carbonyl oxygen atom from an adjacent molecule, thus forming a dimeric $R_4^4(20)$ ring motif (M). Moreover, the perchlorate ion becomes a double H-bond acceptor (from water and ammonium), forming a dimeric $R_6^6(26)$ ring (N). Interconnection between the rings M and N leads the molecules to propagate along [001] direction (Figure 3a), forming an alternate MNMN infinite chain. A second water molecule simultaneously performs as an H-bond donor and acceptor to the carbonyl oxygen atom and ammonium group, respectively, and interconnects the (N) rings along [100] direction. Thus, solvent water molecules play a vital part in forming the supramolecular network structure in (**2**), which spreads on the (101) plane (Figure 3a). Moreover, the solid-state structure of (**2**) shows that the two oxygen atoms of perchlorate anion are oriented toward the π-cloud of the B-ring and A-ring in the molecule. The separation distances between the oxygen atoms and the centroids are 3.396(2) and 3.436(2) Å, respectively. Thus, the perchlorate anion binds the cationic moiety through anion···π[51,52] and anion···π^+ interactions and generates a dimeric molecular moiety (Figure 3b). Finally, the N atoms of the −C ≡ N substituent interact with the centroids of the B-ring and A-ring with a separation distance of 3.817(2) and 3.699(2) Å, respectively. These lp···π[53,54] and lp···π^+ interactions also generate a dimeric motif that propagates along [100] direction (Figure 3c). Interestingly, in the opposite face of the π-clouds of both A and B rings, the O atoms of the perchlorate anion connect the ring centroids through anion···π^+ and anion···π interactions. Thus, two types of lp···π^+/π^+···anion and lp···π/π···anion networks are generated in the solid-state assembly of (**2**) (Figure 3c).

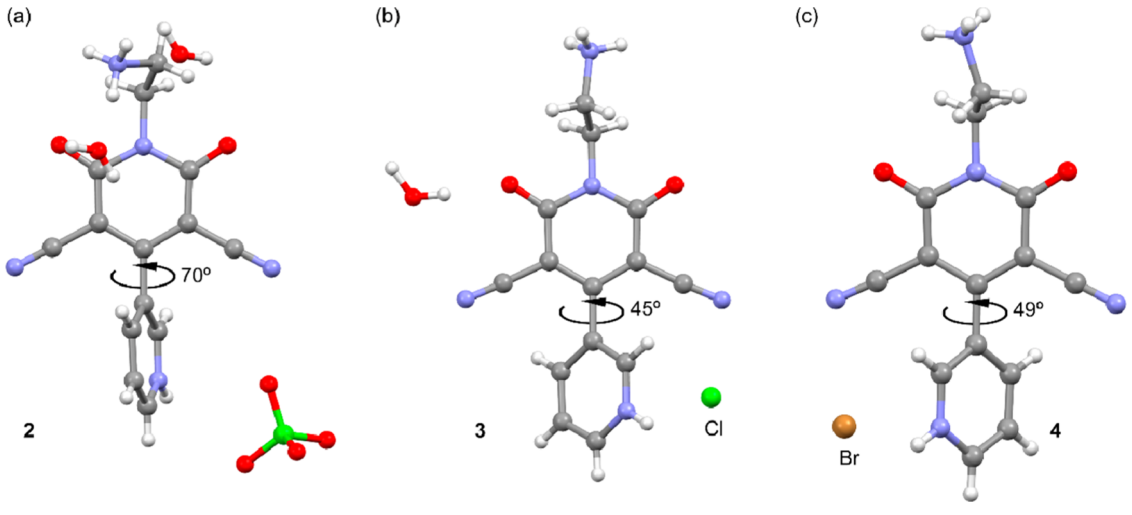

Figure 2. X-ray structures of compounds (**2**–**4**) (a–c, respectively) with indication of the bis-arene torsion angle.

DOI: 10.1021/acsomega.9b00289
ACS Omega 2019, 4, 7200−7212

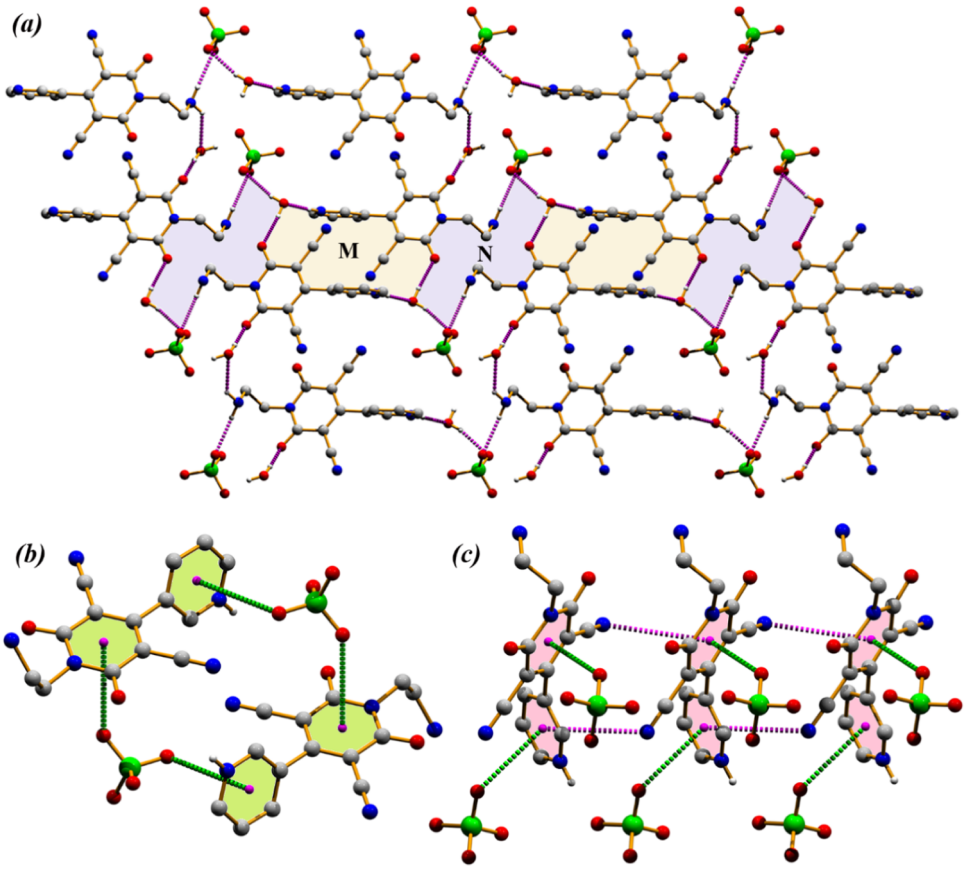

Figure 3. (a) Formation of a two-dimensional (2D) network through multiple ring motifs, (b) dimeric unit generated through mutual anion···π and anion···π^+ interaction, and (c) perspective view of the lp···π^+/π^+···anion and lp···π/π···anion network in (**2**).

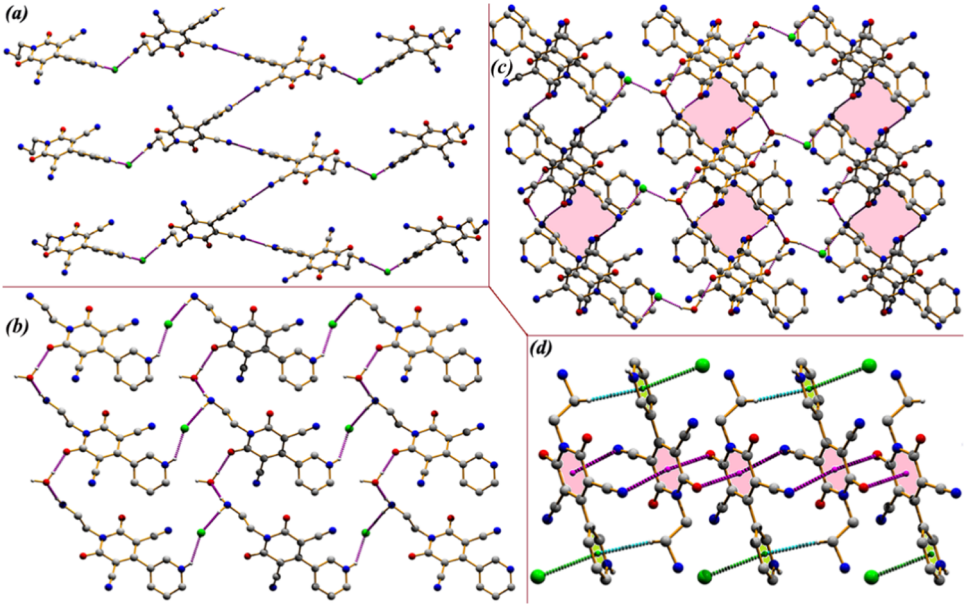

Figure 4. (a) Formation of a layer in (011) plane, (b) network generated in (101) plane, (c) supramolecular framework in (101) plane, and (d) network through multiple lp···π interactions and anion···π^+ interactions in (**3**).

The crystal structure of (**3**) is stabilized through N−H···Cl, O−H···Cl, N−H···N, N−H···O, O−H···O, C−H···N, C−H···O hydrogen bonds, π···π stacking, lp···π, and anion···π^+ interactions (Tables S2−S4). The protonated pyridine ring nitrogen atom N(1) acts as an H-bond donor to N(4) that governs the generation of an infinite one-dimensional zigzag chain along [010] direction. On both sides of this chain, the Cl ion acts as a double H-bond acceptor to the protonated pyridine nitrogen atom and ammonium group. The interconnection of the N−H···N and N−H···Cl bonds directs the molecules to form a two-dimensional network in (011) plane (Figure 4a). Furthermore, the interconnection between

DOI: 10.1021/acsomega.9b00289
ACS Omega 2019, 4, 7200−7212

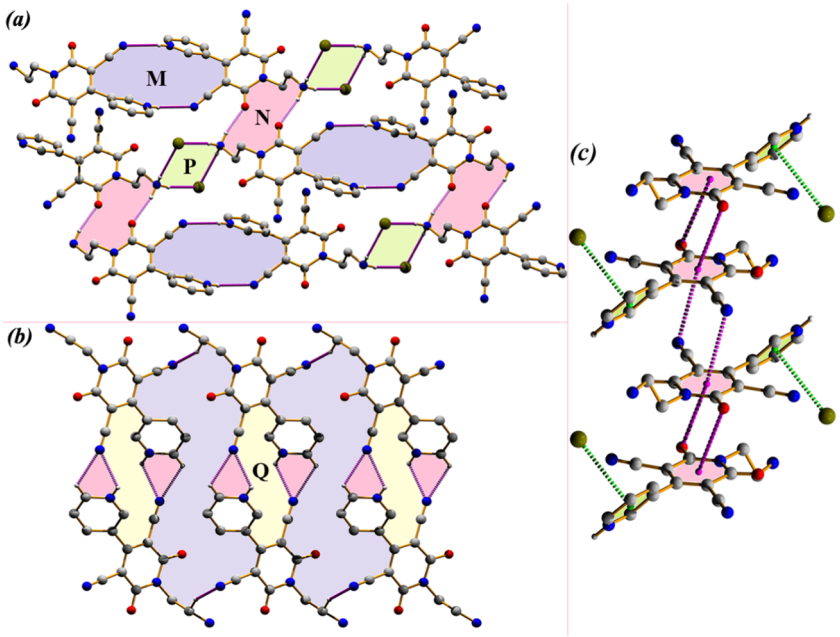

Figure 5. (a) Formation of centrosymmetric dimeric motifs and a two-dimensional assembly, (b) dimeric and tetrameric motifs as a building block of the two-dimensional assembly, and (c) lp···π/π···lp network in (**4**).

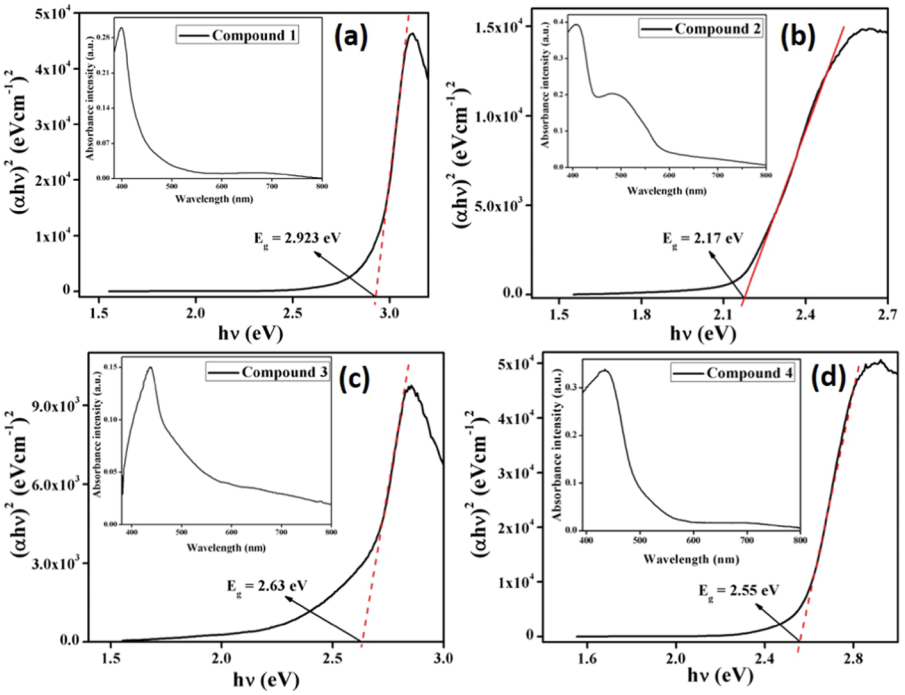

Figure 6. UV−vis spectra (inset) and Tauc's plots for compounds (**1**−**4**) (a−d, respectively).

pyridine nitrogen and amine nitrogen atoms with chlorine anion and the role played by the water oxygen atom generate a different supramolecular framework in (101) plane (Figure 4b). The ammonium group acts as an H-bond donor to the carbonyl oxygen atom, forming a centrosymmetric $R_2^2(14)$ ring (Figure 4c). In both sides of this dimeric unit, chloride ion acts as a double H-bond acceptor and a water molecule acts as a double H-bond donor, forming a two-dimensional supramolecular framework in (101) plane (Figure 4c). Furthermore, the carbonyl oxygen is in contact with the centroid of the ring-B with a separation distance of 3.955(2) Å, revealing the formation lp···π interactions in (**3**) (Figure 4d). Interestingly, on both sides of the dimer, cyano N-atom forms lp···π interaction with the B-ring, with a separation distance of 3.111(3) Å. The combination of O···π and N···π leads the molecules to form an infinite lp···π/π···lp network (Figure 4d). Finally, one C−H bond is in contact with the centroid of ring-A, forming a C−H···π^+ interaction, and in the opposite side of the ring, the chloride ion is oriented toward the π-face of the ring, establishing an anion···π^+ interaction with a separation distance of 3.422(2) Å.

DOI: 10.1021/acsomega.9b00289
ACS Omega 2019, 4, 7200−7212

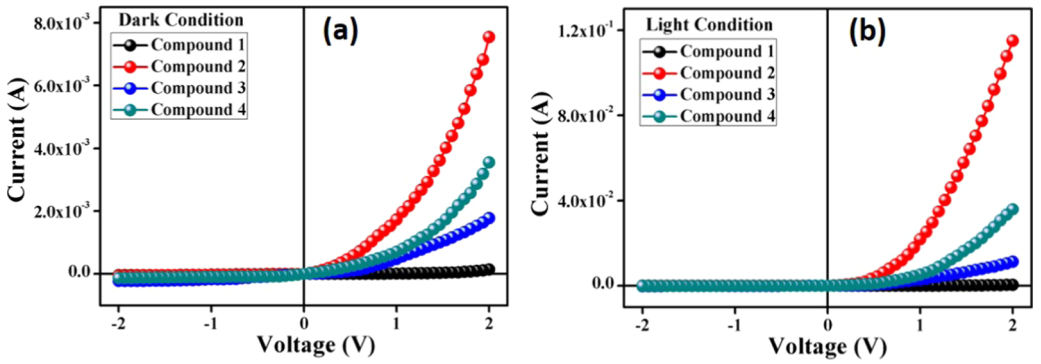

Figure 7. *I*−*V* characteristic curve for indium tin oxide/compound (**1**−**4**)/Al structured thin-film devices under (a) dark and (b) illumination conditions.

The molecules of (**4**) exhibit N−H···Br, N−H···N, N−H···O, C−H···Br, C−H···N, and C−H···O hydrogen bonds and $\pi\cdots\pi$ stacking and lp···π and anion···π^+ interactions (Tables S2−S4). The protonated pyridine N atom acts as an H-bond donor to one CN group, generating a centrosymmetric $R_2^2(16)$ dimeric ring (M) (Figure 5a). On both sides of the dimeric ring motif, the ammonium group acts as an H-bond donor to the carbonyl oxygen atom, forming a centrosymmetric $R_2^2(14)$ dimeric ring (N) (Figure 5a). Bifurcated H-bonding interactions are established between the RNH_3^+ groups and the Br^- ion to form the P-type dimer with a characteristic $R_4^2(8)$ ring (Figure 5a). Thus, the interconnection of the zero-dimensional dimeric ring motifs M, N, and P guides the molecules to form a 2D supramolecular network in (**4**) (Figure 5a). Moreover, a centrosymmetric $R_2^2(18)$ dimeric ring (Q) is generated through the formation of bifurcated C−H···NC and N−H···NC interactions (Figure 5b). Additional reinforcement between the molecules is given by a pair of C−H···N H bonds (Q-motifs, see Figure 5b) to form a tetrameric network. Interconnection of the dimeric and tetrameric ring motifs leads the molecules to propagate a network structure in (101) plane. The molecular packing in (**4**) also shows the formation of lp···π interactions. That is, the carbonyl oxygen atom is oriented toward the π-cloud of the B-ring with a separation distance of 3.519(6) Å (to the ring centroid), thus forming a dimer. At the opposite side of the ring, the N atom also establishes an lp···π interaction with B ring; N···Cg(B) separation distance is 3.413(6) Å. The occurrence of these two lp···π contacts produces an lp···π/π···lp network by interconnecting two dimers in (**4**) (Figure 5c). Moreover, the Br atom establishes an anion···π^+ interaction with ring A with a separation distance of 3.712(2) Å.

Optical Characterization. For optical characterization, thin films of compounds (**1**−**4**) were prepared on normal glass substrate from the stable dispersion of the compounds in dimethyl formamide. Solid-state UV−vis spectra of the films (inset, Figure 6) were recorded for the determination of optical band gaps. Direct optical band gaps were calculated using Tauc's equation[55] (eq S1); the values were found to be 2.92, 2.17, 2.63, and 2.55 eV (Figure 6) for (**1**−**4**), respectively.

Electrical Characterization. Calculated optical band gaps of (**1**−**4**) resemble the semiconducting nature of the compounds. Therefore, metal (Al)−semiconductor (our prepared compounds) (MS) junction thin-film devices have been fabricated. To study the electrical parameters of the devices, we have analyzed the charge transport behavior through the MS junction. The current−voltage (*I*−*V*) characteristics of (**1**−**4**)-based multiple devices, measured with a Keithley 2635B sourcemeter under dark conditions with AM 1.5 G at the corresponding applied bias voltage sequentially within the limit ±2 V are presented in Figure 7a,b.

Under dark conditions, estimated conductivity values for (**1**−**4**)-based devices were found to be 1.14×10^{-6}, 2.33×10^{-4}, 5.27×10^{-5}, and 9.55×10^{-5} (respectively, in S m^{-1}), representative of a semiconductor. On the other hand, under illumination, the estimated conductivities became 4.48×10^{-6}, 2.33×10^{-3}, 1.66×10^{-4}, and 5.93×10^{-4} (in S m^{-1}) for (**1**−**4**)-based devices, respectively, showing a significant enhancement of conductivity in all devices under irradiation conditions. Besides, the obtained *I*−*V* characteristics of the Al/compounds interface under irradiated and nonirradiated conditions exhibit a nonlinear rectifying nature representing the distinct characteristic of a Schottky barrier diode (SBD). Under dark conditions, the rectification ratio (I_{on}/I_{off}) of the SBDs has been determined as 3.41, 35.26, 7.83, and 26.45, respectively; whereas under illumination condition, the values were 9.43, 94.14, 41.32, and 68.21 for (**1**−**4**)-based devices, respectively. The larger current under irradiation condition clearly represents the photoresponse of the devices, which has been measured as 2.71, 15.23, 5.76, and 10.11 for (**1**−**4**)-based SBDs, respectively.

With the help of thermionic emission theory, the *I*−*V* characteristics of (**1**−**4**)-based SBDs were analyzed. To extract important diode parameters, here we have employed Cheung's method.[55] Using eqs 1 and 2, we analyzed *I*−*V* curves quantitatively[55,56]

$$I = I_0 \exp\left(\frac{qv}{\eta kT}\right)\left[1 - \exp\left(\frac{-qv}{\eta kT}\right)\right] \quad (1)$$

$$I_0 = AA^*T^2 \exp\left(\frac{-q\varnothing_B}{kT}\right) \quad (2)$$

where I_0, k, T, V, A, η, and A^* stand for saturation current, electronic charge, Boltzmann constant, temperature in Kelvin, forward bias voltage, effective diode area, ideality factor, and effective Richardson constant, respectively. In this work, the effective diode area has been estimated as 7.065×10^{-2} m^2 and the effective Richardson constant has been considered as 32 A K^{-2} cm^{-2} for all devices.

We also determined some important device parameters, like the ideality factor (η), series resistance (R_S), and barrier potential height ($\varnothing_B$) using Cheung's equations[57,58] (eqs S2−S4). The η values for all devices under dark and illumination

DOI: 10.1021/acsomega.9b00289
ACS Omega 2019, 4, 7200−7212

Table 1. Schottky Device Parameters of Compounds (1−4)-Based SBDs

device	condition	on/off	conductivity (S m^{-1})	photosensitivity	ideality factor	barrier height (eV)	R_S from $dV/d(\ln I)$ (kΩ)	R_S from H (kΩ)
(1)	dark	3.41	1.14×10^{-6}	2.71	3.48	0.42	33.85	32.59
	light	9.43	4.48×10^{-6}		3.19	0.41	32.09	30.49
(2)	dark	35.26	2.33×10^{-4}	15.23	2.35	0.36	2.41	2.09
	light	94.14	2.33×10^{-3}		1.44	0.32	0.89	0.82
(3)	dark	7.83	5.27×10^{-5}	5.76	3.11	0.40	6.19	5.95
	light	41.32	1.66×10^{-4}		2.49	0.36	2.74	2.44
(4)	dark	26.45	9.55×10^{-5}	10.11	2.83	0.39	5.11	4.61
	light	68.21	5.93×10^{-4}		2.04	0.35	2.11	1.94

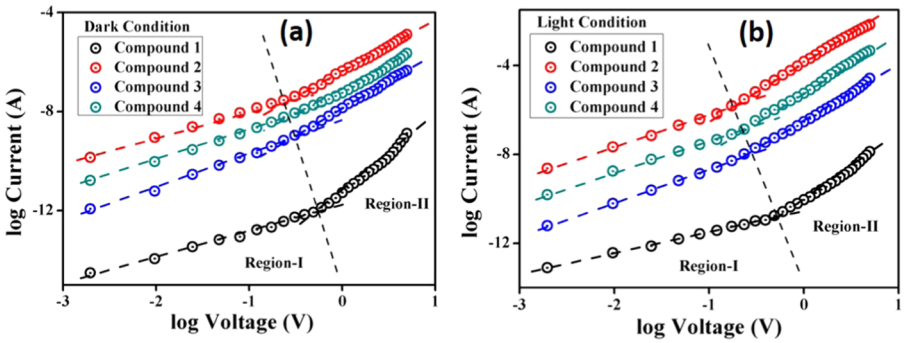

Figure 8. Typical $I-V$ curves for the compound (1−4)-based thin-film devices under (a) dark condition and (b) under illumination condition.

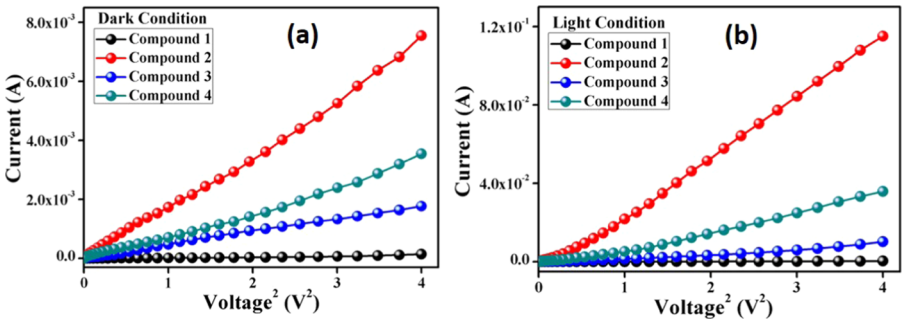

Figure 9. I vs V^2 curves for the compound (1−4)-based thin-film devices (a) under dark condition and (b) under illumination condition.

conditions have been computed from the intercept of $dV/d(\ln I)$ vs I plot (Figure S2, Table 1). The values of η were found to be 3.48, 2.35, 3.11, and 2.83 under the dark condition for (1−4)-based SBDs, respectively, whereas under illumination condition, the values became 3.19, 1.44, 2.49, and 2.04 for (1−4)-based SBDs, respectively. A deviation in η from the ideal value (1) is thus apparent under both conditions. The presence of inhomogeneities in Schottky barrier height and existence of interface states and series resistance at the junction may be the major factors responsible for this deviation.[59,60] Here, the notable point is that the values of η for all SBDs approached a more ideal value (closer to 1) under irradiation condition, indicating less interfacial charge recombination and better homogeneity of Schottky junctions.[55] Moreover, η values associated with a compound (2)-based device become more ideal than those associated with other devices. This observation implies that compound (2) possesses less carrier recombination at the junction, i.e., better barrier homogeneity, even under illumination condition than all other synthesized compound-based devices.

R_S values have been measured from the slope of $dV/d(\ln I)$ vs I plot (Figure S2). Using just the obtained η values in the eq S4, we have determined Φ_B from the intercept of H vs I plot (Figure S3) and Φ_B is found to reduce under irradiation condition for all compound-based SBDs. The generation of photoinduced charge carriers and their accumulation near the conduction band may be the reason of this decrement in Φ_B. The measured values of η, Φ_B, and R_S under both dark and illumination conditions for the metal (Al)−semiconductor (MS) junctions are provided in Table 1. The obtained R_S value from the slope of H vs I plot (Figure S3) is also found to decrease upon light illumination (Table 1), indicating the applicability of the synthesized compounds in optoelectronic devices. In this context, optical band gap and electrical conductivity data of some recently reported organic compounds along with our synthesized compounds are listed in Table S5. Comparing these values, it can be concluded that our reported 4-aryl-2-pyridone derivatives have potential for implementation in various optoelectronic devices.

A detail analysis of the $I-V$ curves is required for a better understanding of the charge transport phenomena at the MS interface. The characteristic $I-V$ curves on the logarithm scale under both conditions can be divided in two distinct slopes (Figure 8, region I and II).

Region−I refers to the Ohmic regime; here, the slope is nearly 1 ($I \propto V$); in Region−II, the slope is nearly 2 with I

DOI: 10.1021/acsomega.9b00289
ACS Omega 2019, 4, 7200−7212

Table 2. Charge-Conducting Parameters of the Compound (1−4)-Based Thin-Film Devices

device	condition	ε_r	μ_{eff} (m^2 V^{-1} s^{-1})	τ (s)	$\mu_{eff}\tau$	D	L_D (m)
(1)	dark	1.52×10^{-1}	3.16×10^{-11}	7.39×10^{-3}	2.33×10^{-13}	7.91×10^{-13}	1.08×10^{-7}
	light		8.65×10^{-11}	2.65×10^{-3}	2.29×10^{-13}	2.16×10^{-12}	1.07×10^{-7}
(2)	dark	7.61×10^{-1}	2.69×10^{-10}	1.95×10^{-3}	2.98×10^{-13}	6.72×10^{-12}	1.22×10^{-7}
	light		4.18×10^{-9}	2.59×10^{-4}	3.14×10^{-13}	10.45×10^{-11}	1.25×10^{-7}
(3)	dark	3.08×10^{-1}	1.32×10^{-10}	2.35×10^{-3}	2.57×10^{-13}	3.31×10^{-12}	1.13×10^{-7}
	light		1.06×10^{-9}	2.73×10^{-4}	2.74×10^{-13}	2.65×10^{-11}	1.17×10^{-7}
(4)	dark	4.09×10^{-1}	2.51×10^{-11}	1.08×10^{-3}	2.70×10^{-13}	6.25×10^{-12}	1.16×10^{-7}
	light		2.66×10^{-9}	1.11×10^{-4}	2.95×10^{-13}	6.65×10^{-11}	1.21×10^{-7}

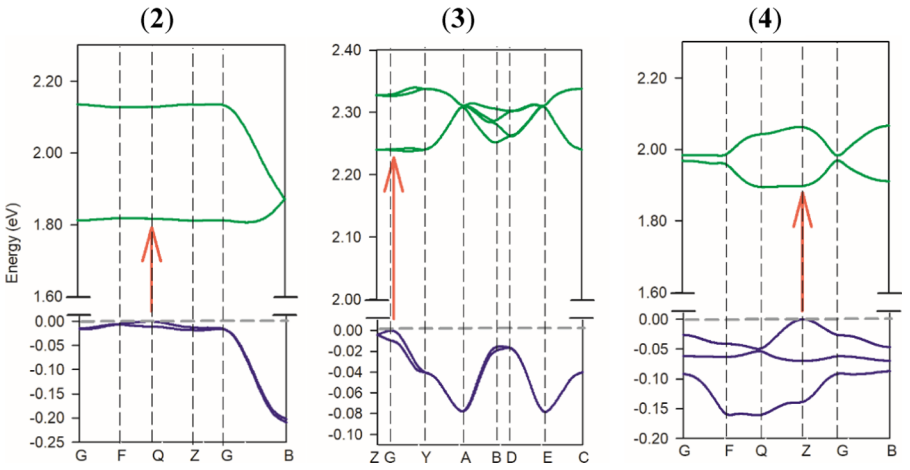

Figure 10. Electronic band structures of compounds (**2**), (**3**), and (**4**). High-symmetry points are labeled as follows: (**2**) and (**4**): G = (0, 0, 0); F = (0, 0.5, 0); Q = (0, 0.5, 0.5); Z = (0, 0, 0.5); B = (0.5, 0, 0) (**3**): Z = (0, 0, 0.5); G = (0, 0, 0); Y = (0, 0.5, 0); A = (−0.5, 0.5, 0); B = (−0.5, 0, 0); D = (−0.5, 0, 0.5); E = (−0.5, 0.5, 0.5); C = (0, 0.5, 0.5).

proportional to V^2 (Figure 8), representing the characteristic of a trap-free space charge-limited current (SCLC) regime.[55,61] The SCLC theory was used here to estimate the mobility of materials.[55,61]

This model was followed to estimate the effective carrier mobility from the higher voltage region of the I vs V^2 plot (Figure 9), applying the Mott−Gurney equation[55,58,61]

$$I = \frac{9\mu_{eff}\varepsilon_0\varepsilon_r A}{8}\left(\frac{V^2}{d^3}\right) \quad (3)$$

where I refers to the current, ε_0 is the permittivity of free space, ε_r is the relative dielectric constant of the synthesized material, and μ_{eff} is the effective dielectric constant.

The capacitance against frequency plot at a constant bias potential (Figure S4) clearly shows a tendency of saturation of the capacitance in the higher frequency regime. From this regime, the capacitance was found to be 9.51×10^{-12}, 4.76×10^{-11}, 1.93×10^{-11}, and 2.56×10^{-11} F for (**1**−**4**), respectively. The dielectric permittivity of the films was calculated (eq S5) as 1.52×10^{-1}, 7.61×10^{-1}, 3.08×10^{-1}, and 4.09×10^{-1} for (**1**−**4**), respectively. To explore charge transport across the junction, a few more key parameters, like transit time (τ) and diffusion length (L_D), have also been estimated (eqs S6−S8). The L_D of charge carriers plays a significant function in device performance when a metal semiconductor junction is formed. The estimated values of all parameters in the SCLC region exhibit an improvement of charge transport properties after light soaking (Table 2). The higher mobility suggests a greater transport rate and increase in the number of charge carriers under irradiation condition, whereas increased L_D under light condition suggests that the charge carriers travel longer before their recombination, which is responsible for the eventual increase in the current displayed by the device under light. It is worthy to mention here that the compound (**2**)-based SBD shows the best performance compared with other devices (diode parameters are given in Table 2). Compound (**2**)-based SBDs also exhibit much enhanced charge-transfer kinetics after light soaking. So, this class of compounds can be utilized in device application.

Theoretical Analysis. The band gaps measured for compounds (**2**−**4**) from the experiment using Tauc's plot range from 2.17 to 2.63 eV. Thus, the anion has a small influence on the band gap value. However, appreciable differences in the electrical properties of the materials have been found when they are in the dark or when they are irradiated with light. The theoretical calculations are carried out to analyze the influence of the counterions upon the optical characteristics of the compounds. The density functional theory (DFT) calculations used in this work permit us to study the properties inherent to each of these materials. However, it should be mentioned that other effects can also affect the results of the experiments, like defects, interfaces, impurities, thickness of the semiconductor layer, excitons, etc., which are obviously not considered in this DFT study. The experimental crystal coordinates have been used as the initial geometries for the DFT calculations. Standard band theory along with partial density of state (PDOS) calculations has been employed for the analysis of the properties of the optimized structures. The plot of the Kohn−Sham electronic energy levels as a function of the reciprocal space vector k has

DOI: 10.1021/acsomega.9b00289
ACS Omega 2019, 4, 7200−7212

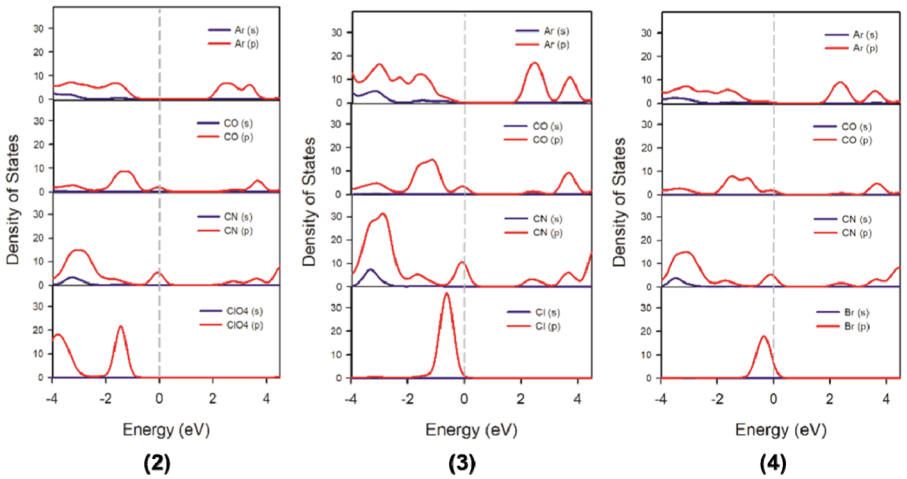

Figure 11. Left: PDOS of aromatic atoms (Ar), ketone group (CO), nitrile (CN), and perchlorate (ClO_4^-) of (**2**). Middle: PDOS of aromatic atoms (Ar), ketone (CO), nitrile (CN), and chloride (Cl^-) of (**3**). Right: PDOS of aromatic atoms (Ar), ketone (CO), nitrile (CN), and bromide (Br^-) of (**4**) crystal cell.

been made using the first Brillouin zone, where the selected path crosses high-symmetry points (see Figure 10).

These results confirm that compounds **2**–**4** are semiconductors (Figure 10). Compound (**2**) and (**4**) crystallize as $P\bar{1}$ triclinic crystals and compound (**3**) crystallizes as $P2_1/c$ monoclinic crystal, and the theoretical band gaps are 1.81, 1.90, and 2.23 eV for compounds (**2**), (**4**), and (**3**), respectively. Previous works have shown that semiconductor band gap values are underestimated by the DFT method.[62,63] However, it is widely accepted that the form of the bands is accurate. The results from Figure 10 confirm that all compounds are direct-type semiconductors. Moreover, the experimental trends agree well with the DFT results. Specifically, compound (**2**) exhibits the lowest band gap (2.17 eV), and compound (**3**), the largest one (2.63 eV).

In Figure 11, we represent the partial density of states of compounds **2**–**4**. This type of plot allows us to understand which atoms are responsible for the electrical conductivity since the transport phenomenon is caused by the e^-s located at the outermost shells. For compounds (**2**) and (**3**), the PDOS calculation reveals that 2p orbitals of ketone and nitrile groups dominate in the uppermost valence bands. In addition, the 2p orbitals of the aromatic ring dominate in the bottom-most conduction bands. Neither perchlorate nor chloride has any levels present in those bands. In contrast, in compound (**4**), in addition to 2p orbitals of the CO and CN groups, the 4p orbitals of bromine anion also participate on top of the valence energy levels. This study indicates that the role of the anion is more related to structural changes (crystal packing) that they produce in the 3D architecture of the compounds than their direct participation in the valence and conduction bands. This behavior has been previously described in perovskites[64,65] and in pyridone-based organic salts.[66]

The analysis of the optical properties is needed to rationalize the electronic structure of the crystal structure. The computation of the dielectric function $\varepsilon(\omega)$ and the optical conductivity $\sigma(\omega)$ is convenient to study how frequently the photon is absorbed into the material. The real part of the former correlates with the degree of polarization of the material after the application of the electric field, and the imaginary part correlates with the photon absorption. The latter, $\sigma(\omega)$, is useful to analyze how the illumination affects the conductivity.

The optical properties have been computed (see Figure 12a) using a photon energy that ranges from 0 to 16 eV. The peaks represent electronic transitions from the valence band to the conduction band (uppermost band of the valence bands to the bottom-most band of the conduction bands). The dielectric constant has been decomposed in three main directions (ε_{xx}, ε_{yy}, and ε_{zz}) where the incident light strikes the product. In compound (**2**), the optical absorption begins at 1.72 eV in the three directions (Figure 12, left). It represents the greatest anisotropy of all three compounds studied theoretically, finding different profiles depending on the direction of incidence of light on the glass. In the "*y*" and "*z*" directions (ε_{yy} and ε_{zz}, green and red lines, respectively), it presents maximum peaks in approximately 2.04, 3.32, 4.02, 5.40, and 8.04 eV into the 1.6–10.5 eV range. On the other hand, the "*x*" direction (ε_{xx}, blue line) presents maximum peaks at 2.67, 3.28, 5.36, and 8.02 eV. The band structure in compound (**3**), which exhibits the highest band gap value of the three compounds, shows that the peaks in all directions of polarization of light have similar width but quite different intensity. The first and least intense maximum peaks in the three directions fall at ~2.58 eV. Other maximum peaks can be observed at 3.94, 5.22, and 7.95 eV. Finally, (**4**) has one preferred absorption range with maximums at 2.53, 3.91, 5.36, and 8.45 eV in the directions ε_{xx} (blue line) and ε_{zz} (red line) of the incident light. Moreover, the behavior of the optical conductivity (Figure 12b) is similar to that presented by the dielectric constant. These results demonstrate that only selected wavelengths exhibit an optical response. In our case, compound (**2**) begins to absorb at 1.60 eV with maximums peaks at 2.0, 2.6, 2.7, 3.3, 4.0, 5.4, 6.5, and 8.1 eV, therefore being more disposed to the absorption of light than (**3**) and (**4**), which begin to absorb at 1.8 and 1.77 eV, respectively. These results along with a lower band gap of **2** explain the larger electrical conductivity of this crystal and its increment upon illumination.

DNA Interaction Results and Discussions. DNA binding study was carried out with compound (**2**) representative of others. MOE program predicted that the compound partially intercalates into the DNA base pairs (Table S6, Figure 13) and the free energy of binding was

DOI: 10.1021/acsomega.9b00289
ACS Omega 2019, 4, 7200–7212

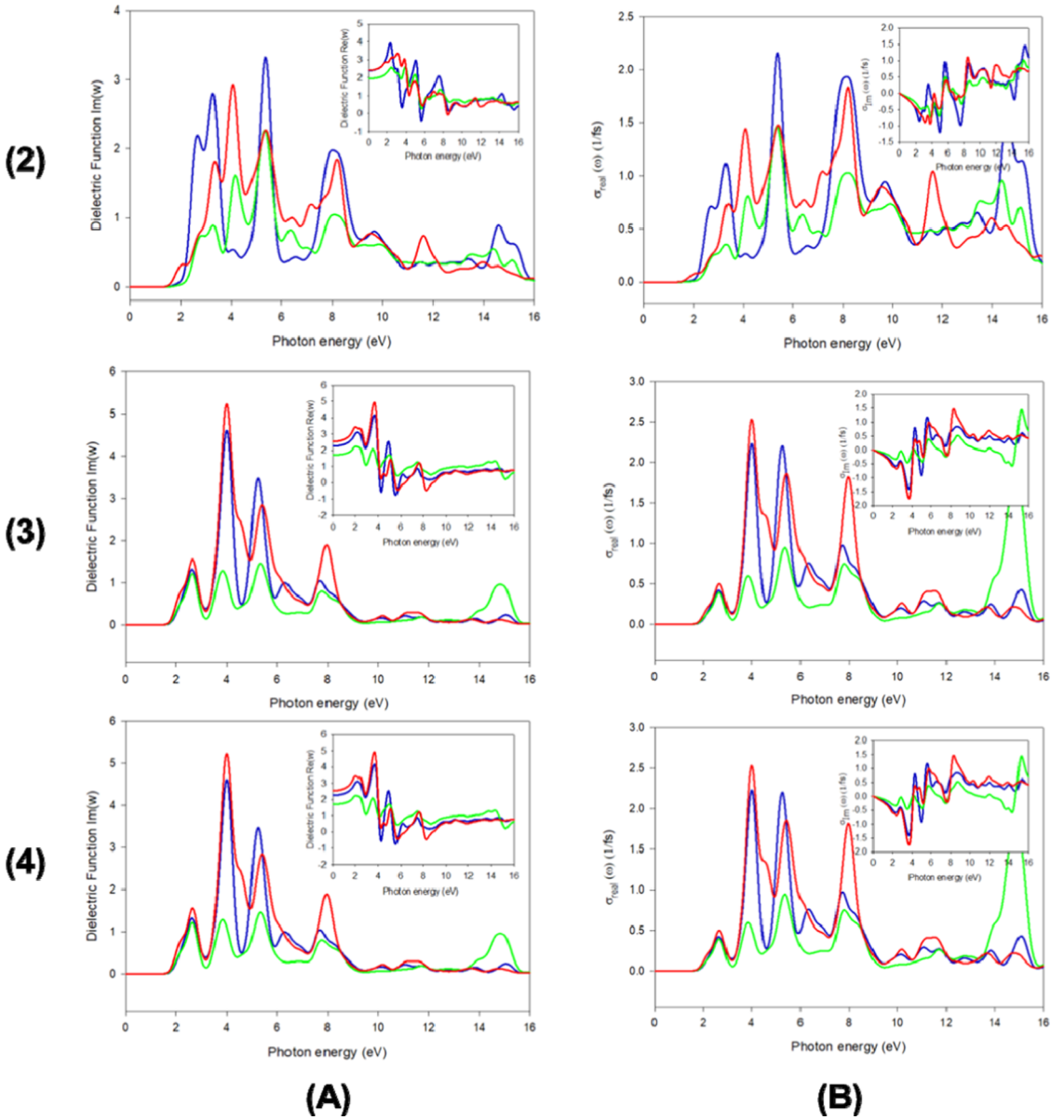

Figure 12. (A) Plot of imaginary and real (inset plot) parts of the dielectric function vs the photon energy of compounds (**2**–**4**). Blue, green, and red lines correspond to "*x*", "*y*", and "*z*" directions of the incident radiation, respectively. (B) Plot of real and imaginary (inset plot) parts of optical conductivity vs the photon energy. Blue, green, and red lines correspond to "*x*", "*y*", and "*z*" directions of the polarized radiation, respectively.

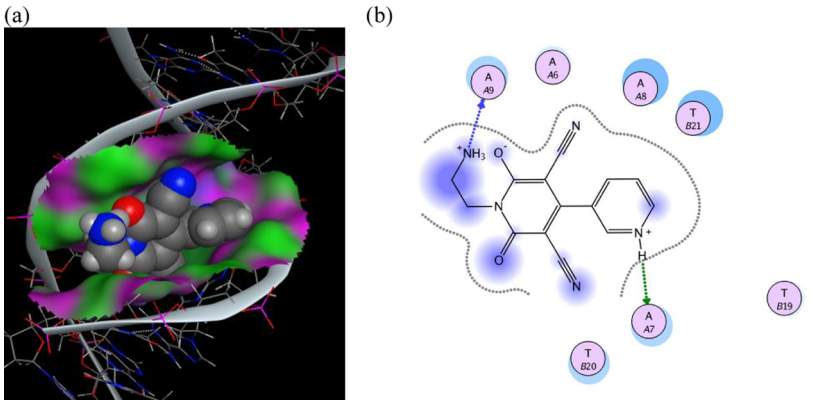

Figure 13. (a) Representative picture for partial intercalation of the compound into DNA base pair, and (b) two-dimensional picture for the binding of cationic 3-pyridinyl-2-pyridone moiety with DNA.

DOI: 10.1021/acsomega.9b00289
ACS Omega 2019, 4, 7200−7212

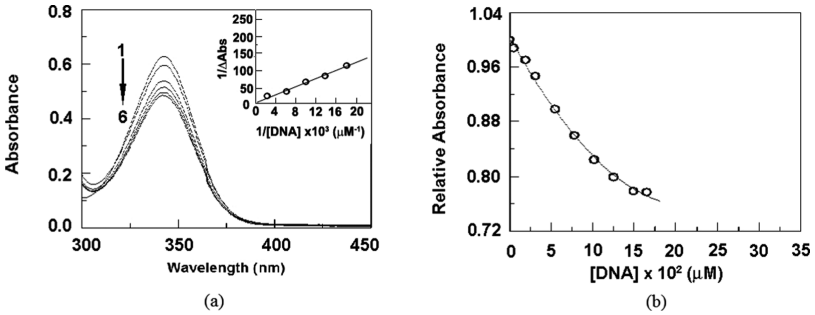

Figure 14. (a) Absorbance spectra of 34 μM compound **2** in presence of 0, 196, 294, 417, 540, and 620 μM DNA (curves 1−6) (inset: Benesi−Hildebrand plot) and (b) relative absorbance change with increasing concentration of DNA.

estimated as −4.70 to −5.30 kcal mol^{-1}, in agreement with UV−vis spectroscopic studies. During the binding, numerous hydrogen bonds created between DNA bases and some specific groups of cationic moiety, like "O", "N" of CN, and NH_3^+ group, give the system extra stability.

Circular dichroic (CD) spectral study supports the predicted conformational free energy, which was found to be ∼0.8 kcal mol^{-1}.

Spectroscopic Result. Figure 14 shows how changes in the concentration of CT-DNA affect the absorption spectra of the compound (**2**); the absence of any isosbestic point in the spectra may be due to the larger molar extinction coefficient of (**2**) over that of the compound−DNA complex, formed during binding.[66,68]

The binding constant of the compound was determined using the Benesi−Hildebrand plot[67] (Figure 14, inset) and was found to be 9.21 × 10^2 M^{-1}.

CD experiment was carried out to examine if there appears any conformational change of DNA during the binding. DNA exhibits a positive band near 270 nm and a negative band near 240 nm, indicating B-form conformation of DNA. During the binding, changes in both positive and negative bands were observed (Figure 15). The change in the positive band

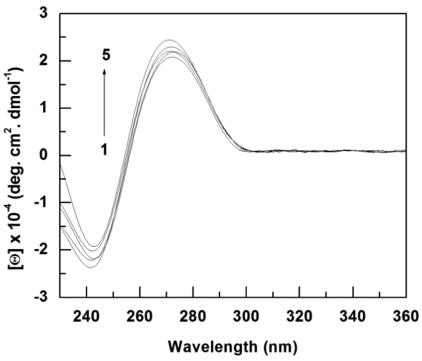

Figure 15. Intrinsic CD spectra of CT DNA (60 μM) in the presence of 0, 6, 12, 18, and 30 μM compound (**2**).

represents that stacking between base pairs decreased, whereas the alteration in the conformation of DNA helix (unwinding) was predicted by change in the negative band.

CONCLUSIONS

In summary, we have synthesized an organic compound and three of its salts and established the crystal structures of the salts. Detailed explorations of optical and electrical properties illustrate the semiconducting nature and photoresponse behavior of the parent organic compound and its salts. Electrical properties after salt formation are enhanced significantly as compared to those of the parent compound. Exposure to visible light improves the electrical conductivity of all compounds, but this improvement is the maximum in the case of the perchlorate salt of compound (**1**). Theoretical studies established these observations. These organic salts can add a new dimension in the extensive research field of optoelectronic devices and in organic semiconducting industries. The DNA binding ability of one of the representative salts was also checked, and it was observed that the compound can bind to DNA helix in a partial intercalative manner.

EXPERIMENTAL SECTION

Materials and Measurements. Chemicals (reagent grade) were purchased from Sigma-Aldrich Co. Freshly boiled doubly distilled water was used for synthesis purposes. IR spectra in the range of 4000−400 cm^{-1} were recorded using a Perkin-Elmer RXI FT-IR spectrophotometer. Elemental analyses (percentages of C, H, and N) were performed on a Perkin-Elmer 240 C elemental analyzer. ^{1}H NMR spectra of compound (**1**) was recorded on a Bruker 300 MHz instrument using deuterated dimethyl sulfoxide (DMSO). The HRMS QTOF Micro YA263 mass spectrometer was used to obtain mass spectra of (**1**). A Rigaku-TTRAX-III diffractometer (Cu Kα radiation (λ = 1.5406 Å)) was used to collect powder X-ray diffraction (PXRD) data of the compounds (**2**−**4**). Figure S5 compares the PXRD pattern of the salts (**2**−**4**) with their simulated pattern.

Synthesis of (1). The organic compound (**1**) was synthesized following a literature method.[69] 3-Pyridinecarboxaldehyde (1 g, 9.35 mM), ethylcyanoacetate (2.32 g, 20.51 mM), and ethylenediamine (0.616 g, 10.25 mM) were refluxed in ethanol for 2 h to get the desired product (**1**); it was filtered and washed thoroughly with hot water. Several efforts to crystallize (**1**) in different solvents were unsuccessful (Table S7). Characterization of compound (**1**) was done by IR, ^{1}H NMR (Figure S6), and mass spectroscopy (Figure S7). Anal. Calcd for (**1**) $C_{14}H_{11}N_5O_2$: C, 59.78; H, 3.94; N, 24.90%. Found: C, 59.60; H, 3.79; N, 25.02%. Main IR absorption bands observed for (**1**) (KBr pellet/cm^{-1}) are 3008 (w), 2211 (s), 1640 (s), 1600 (s), 1550 (s), 1533 (s), 1499 (s), 1449 (s), 1356 (s), 1218 (s), 1155 (s), 1066 (s), 987 (s), 825 (s), 767 (s), 673 (s), 510 (s), 485 (s), 412 (s); ^{1}H NMR (300 MHz, DMSO-d_6) δ in ppm: 8.67 (1H, J = 3.6 Hz, d), 8.59 (1H, s), 7.85 (1H, J = 7.74 Hz, d), 7.54 (1H, J = 5.01 Hz, t), 4.06 (2H, J = 5.34 Hz, t), 2.98 (2H, t); ES + TOF MS: m/z 265.1562 [M + H]$^+$ (calc. for $C_{14}H_9N_4O_2^+$ 265.2463).

DOI: 10.1021/acsomega.9b00289
ACS Omega 2019, 4, 7200−7212

Synthesis of [H(1)]ClO_4·2H_2O (2). Compound (2) was obtained by reacting (1) (1.0 mM, 0.281 g) with $HClO_4$ solution (pH ∼ 0.5, temperature ∼25.0 °C) with stirring for 2 h. The reaction mixture was then filtered, and the filtrate was left unperturbed. After 2 weeks, yellow block-shaped single crystals of (2) were generated, washed repeatedly with water, and dried in air. Anal. Calcd for $C_{14}H_{16}ClN_5O_8$ (2): C, 40.25; H, 3.86; N, 16.76%. Found: C, 40.39; H, 3.92; N, 16.59%. Main IR absorption bands observed for (2) (KBr pellet/cm^{-1}) are 3518 (s), 3182 (w), 2200 (s), 1606 (s), 1573 (s), 1541 (s), 1086 (s), 1047 (s), 779 (s), 682 (s), and 618 (s).

Synthesis of [H(1)]Cl·H_2O (3). Compound (3) was prepared in the same way by reacting an aqueous solution of HCl with (1). Anal. Calcd for $C_{14}H_{14}ClN_5O_3$ (3): C, 50.08; H, 4.20; N, 20.86%. Found: C, 49.88; H, 4.11; N, 21.08%. Main IR absorption bands observed for (3) (KBr pellet/cm^{-1}) are 3377 (w), 3333 (w), 2997 (w), 2881 (w), 2817 (w), 2203 (s), 1635 (s), 1576 (s), 1517 (s), 1478 (s), 1449 (s), 773 (s), 685 (s), 621 (s), 490 (s), and 417 (s).

Synthesis of [H(1)]Br (4). Compound (4) was obtained by dissolving an aqueous suspension of (1) by drop wise adding aqueous HBr solution (pH ∼ 0.5) following the above procedure. Yellow, block-shaped single crystals of (4) were isolated after 2 weeks from the reaction mixture. Anal. Calcd for $C_{14}H_{12}BrN_5O_2$ (4): C, 46.43; H, 3.34; N, 19.34%. Found: C, 46.51; H, 3.22; N, 19.43%. Main IR absorption bands observed for (4) (KBr pellet/cm^{-1}) are 2994 (w), 2912 (w), 2200 (s), 1575 (s), 1522 (s), 1453 (s), 770 (s), 682 (s), 606 (s), 501(s), and 408 (s).

■ ASSOCIATED CONTENT

Supporting Information

The Supporting Information is available free of charge on the ACS Publications website at DOI: 10.1021/acsomega.9b00289.

X-ray crystallography study; crystal data table, ORTEP diagram of cationic moiety; hydrogen-bonding parameters; geometrical parameters for lp···π interactions; geometrical parameters for π···π interactions; optical characterization; device fabrication; electrical characterization; computational details; molecular docking studies; absorbance spectral studies; circular dichroic study; comparison table showing electrical conductivity data; DNA decamer sequences used for docking study; PXRD pattern of the compounds (2−4); ^1H NMR spectra of (1); mass spectrum of (1) and list of solvents used to crystallize (1) (PDF)

Computational data using SHELXL-97, diffraction data (CIF)(CIF)(CIF)

■ AUTHOR INFORMATION

Corresponding Authors

*E-mail: toni.frontera@uib.es (A.F.).
*E-mail: ju_subrata@yahoo.co.in (S.M.).

ORCID

Joaquín Ortega-Castro: 0000-0001-8131-0315
Partha Pratim Ray: 0000-0003-4616-2577
Antonio Frontera: 0000-0001-7840-2139

Notes

The authors declare no competing financial interest.

■ ACKNOWLEDGMENTS

T.M. gratefully acknowledges the University Grants Commission (New Delhi) for a senior research fellowship. We acknowledge the MINECO/AEI from Spain for financial support (project number CTQ2017-85821-R, FEDER funds). We are grateful to the CTI (UIB) for free allocation of computer time.

■ REFERENCES

(1) Huitema, H. E. A.; Gelinck, G. H.; van der Putten, J. B. P. H.; Kuijk, K. E.; Hart, C.; Cantatore, E.; Herwigm, P. T.; van Breemen, A. J. J. M.; Leeuw, D. M. Plastic transistors in active-matrix displays. *Nature* **2001**, *414*, 599.

(2) Crone, B.; Dodabalapur, A.; Lin, Y. Y.; Filas, R. W.; Bao, Z.; LaDuca, A.; Sarpeshkar, R.; Katz, H. E.; Li, W. Large-scale complementary integrated circuits based on organic transistors. *Nature* **2000**, *403*, 521−523.

(3) Dimitrakopoulos, C. D.; Malenfant, P. R. Organic thin film transistors for large area electronics. *Adv. Mater.* **2002**, *14*, 99−117.

(4) Sirringhaus, H. 25th Anniversary Article: Organic Field-effect Transistors: The Path beyond Amorphous Silicon. *Adv. Mater.* **2014**, *26*, 1319−1335.

(5) Krebs, F. C.; Gevorgyan, S. A.; Alstrup, J. A Roll-to-Roll Process to Flexible Polymer Solar Cells: Model Studies, Manufacture and Operational Stability Studies. *J. Mater. Chem.* **2009**, *19*, 5442−5451.

(6) Gupta, S. K.; Jha, P.; Singh, A.; Chehimi, M. M.; Aswal, D. K. Flexible Organic Semiconductor Thin Films. *J. Mater. Chem. C* **2015**, *3*, 8468−8479.

(7) Reineke, S.; Thomschke, M.; Lüssem, B.; Leo, K. White organic light-emitting diodes: Status and perspective. *Rev. Mod. Phys.* **2013**, *85*, 1245−1293.

(8) Heremans, P.; Gelinck, G. H.; Muller, R.; Baeg, K. J.; Kim, D. Y.; Noh, Y. Y. Polymer and Organic Nonvolatile Memory Devices. *Chem. Mater.* **2011**, *23*, 341−358.

(9) Briand, D.; Oprea, A.; Courbat, J.; Bârsan, N. Making environmental sensors on plastic foil. *Mater. Today* **2011**, *14*, 416−423.

(10) Baeg, K. J.; Binda, M.; Natali, D.; Caironi, M.; Noh, Y. Y. Organic Light Detectors: Photodiodes and Phototransistors. *Adv. Mater.* **2013**, *25*, 4267−4295.

(11) Kumar, B.; Kaushik, B. K.; Negi, Y. S. Organic Thin Film Transistors: Structures, Models, Materials, Fabrication and Applications: A Review. *Polym. Rev.* **2014**, *54*, 33−111.

(12) Naber, R. C. G.; Asadi, K.; Blom, P. W. M.; de Leeuw, D. M.; de Boer, B. Organic Nonvolatile Memory Devices Based on Ferroelectricity. *Adv. Mater.* **2010**, *22*, 933−945.

(13) Dong, H.; Zhu, H.; Meng, Q.; Gong, X.; Hu, W. Organic Photoresponse Materials and Devices. *Chem. Soc. Rev.* **2012**, *41*, 1754−1808.

(14) Pertegás, A.; Tordera, D.; Serrano-Párez, J. J.; Ortí, E.; Bolink, H. J. Light-emitting Electrochemical Cells Using Cyanine Dyes as the Active Components. *J. Am. Chem. Soc.* **2013**, *135*, 18008−18011.

(15) Liu, X.; Jeong, K. S.; Williams, B. P.; Vakhshouri, K.; Guo, C.; Han, K.; Gomez, E. D.; Wang, Q.; Asbury, J. B. Tuning the dielectric properties of organic semiconductors via salt doping. *J. Phys. Chem. B* **2013**, *117*, 15866−15874.

(16) Wang, L.; Jenatsch, S.; Ruhstaller, B.; Hinderling, C.; Gesevičius, D.; Hany, R.; Nüesch, F. Organic Salt Semiconductor with High Photoconductivity and Long Carrier Lifetime. *Adv. Funct. Mater.* **2018**, *28*, No. 1705724.

(17) McManus, P. M.; Cushman, R. J.; Yang, S. C. Influence of oxidation and protonation on the electrical conductivity of polyaniline. *J. Phys. Chem.* **1987**, *91*, 744−747.

(18) Kwon, O.; McKee, M. L. Calculations of band gaps in polyaniline from theoretical studies of oligomers. *J. Phys. Chem. B* **2000**, *104*, 1686−1694.

(19) Whitesides, G. M.; Grzybowski, B. Self-assembly at all scales. *Science* **2002**, *295*, 2418−2421.

DOI: 10.1021/acsomega.9b00289
ACS Omega 2019, 4, 7200−7212

(20) Desiraju, G. R. Supramolecular synthons in crystal engineering-a new organic synthesis. *Angew. Chem., Int. Ed.* **1995**, *34*, 2311−2327.
(21) Zeng, F.; Zimmerman, S. C. Dendrimers in supramolecular chemistry: from molecular recognition to self-assembly. *Chem. Rev.* **1997**, *97*, 1681−1712.
(22) Klok, H. A.; Lecommandoux, S. Supramolecular materials via block copolymer self-assembly. *Adv. Mater.* **2001**, *13*, 1217−1229.
(23) Meng, Y.; Gu, D.; Zhang, F.; Shi, Y.; Cheng, L.; Feng, D.; Wu, Z.; Chen, Z.; Wan, Y.; Stein, A.; Zhao, D. A family of highly ordered mesoporous polymer resin and carbon structures from organic−organic self-assembly. *Chem. Mater.* **2006**, *18*, 4447−4464.
(24) Trask, A. V.; Jones, W. Crystal engineering of organic cocrystals by the solid-state grinding approach. *Top. Curr. Chem.* **2005**, *254*, 41−70.
(25) Dunitz, J. D.; Gavezzotti, A. Molecular recognition in organic crystals: Directed intermolecular bonds or nonlocalized bonding. *Angew. Chem., Int. Ed.* **2005**, *44*, 1766−1787.
(26) Wilkes, J. S.; Zaworotko, M. J. Manifestations of noncovalent interactions in the solid state. Dimeric and polymeric self-assembly in imidazolium salts via face-to-face cation−cation π−stacking. *Supramol. Chem.* **1993**, *1*, 191−193.
(27) Manna, P.; Seth, S. K.; Mitra, M.; Choudhury, S. R.; Bauzá, A.; Frontera, A.; Mukhopadhyay, S. Experimental and computational study of counterintuitive $ClO_4^-\cdots ClO_4^-$ interactions and the interplay between $\pi^+-\pi$ and anion$\cdots\pi^+$ interactions. *Cryst. Growth Des.* **2014**, *14*, 5812−5821.
(28) Das, A.; Jana, A. D.; Seth, S. K.; Dey, B.; Choudhury, S. R.; Kar, T.; Mukhopadhyay, S.; Singh, N. J.; Hwang, I. C.; Kim, K. S. Intriguing π+$-\pi$ Interaction in Crystal Packing. *J. Phys. Chem. B* **2010**, *114*, 4166−4170.
(29) Seth, S. K.; Manna, P.; Singh, N. J.; Mitra, M.; Jana, A. D.; Das, A.; Choudhury, S. R.; Kar, T.; Mukhopadhyay, S.; Kim, K. S. Molecular Architecture Using Novel Types of Noncovalent π-interactions Involving Aromatic Neutrals, Aromatic Cations and π-anions. *CrystEngComm* **2013**, *15*, 1285−1288.
(30) Manna, P.; Seth, S. K.; Mitra, M.; Das, A.; Singh, N. J.; Choudhury, S. R.; Kar, T.; Mukhopadhyay, S. A Successive Layer-by-Layer Assembly of Supramolecular Frameworks Driven by a Novel Type of Face-to-Face $\pi^+-\pi^+$ Interactions. *CrystEngComm* **2013**, *15*, 7879−7886.
(31) Fourmigué, M.; Batail, P. Activation of hydrogen and halogen-bonding interactions in tetrathiafulvalene-based crystalline molecular conductors. *Chem. Rev.* **2004**, *104*, 5379−5418.
(32) Anthony, J. E. The larger acenes: versatile organic semiconductors. *Angew. Chem., Int. Ed.* **2008**, *47*, 452−483.
(33) Anthony, J. E. Functionalized Acenes and Heteroacenes for Organic Electronics. *Chem. Rev.* **2006**, *106*, 5028−5048.
(34) López, J. L.; Atienza, C.; Seitz, W.; Guldi, D. M.; Martín, N. Controlling the Transformation of Primary into Quaternary Structures: Towards Hierarchically Built-Up Twisted Fibers. *Angew. Chem.* **2010**, *122*, 10072−10076.
(35) Kapadia, P. P.; Ditzler, L. R.; Baltrusaitis, J.; Swenson, D. C.; Tivanski, A. V.; Pigge, F. C. Semiconducting organic assemblies prepared from tetraphenylethylene tetracarboxylic acid and bis (pyridine) s via charge-assisted hydrogen bonding. *J. Am. Chem. Soc.* **2011**, *133*, 8490−8493.
(36) Endoh, M.; Hori, M. Acute heart failure: inotropic agents and their clinical uses. *Expert Opin. Pharmacother.* **2006**, *7*, 2179−2202.
(37) Robert, N.; Verrier, C.; Hoarau, C.; Celanire, S.; Marsais, F. A convenient synthesis of cyclopenta[b]pyridin-2,5-dione as a non-glycosidic cardiotonic agent. *Arkivoc* **2008**, *vii*, 92−100.
(38) Lo Presti, E.; Boggia, R.; Feltrin, A.; Menozzi, G.; Dorigo, P.; Mosti, L. 3-Acetyl-5-acylpyridin-2(1H)-ones and 3-acetyl-7,8-dihydro-2,5(1H,6H)-quinolinediones: synthesis, cardiotonic activity and computational studies. *Farmaco* **1999**, *54*, 465−474.
(39) Gupta, A. K.; Plott, T. Ciclopirox: a broad-spectrum antifungal with antibacterial and anti-inflammatory properties. *Int. J. Dermatol.* **2004**, *43*, 3−8.
(40) Dragovich, P. S.; Prins, T. J.; Zhou, R.; Johnson, T. O.; Hua, Y.; Luu, H. T.; Sakata, S. K.; Brown, E. L.; Maldonado, F. C.; Tuntland, T.; Lee, C. A.; Fuhrman, S. A.; Zalman, L. S.; Patick, A. K.; Matthews, D. A.; Wu, E. Y.; Guo, M.; Borer, B. C.; Nayyar, N. K.; Moran, T.; Chen, L.; Rejto, P. A.; Rose, P. W.; Guzman, M. C.; Dovalsantos, E. Z.; Lee, S.; McGee, K.; Mohajeri, M.; Liese, A.; Tao, J.; Kosa, M. B.; Liu, B.; Batugo, M. R.; Gleeson, J. R.; Wu, Z. P.; Liu, J.; Meador, J. W.; Ferre, R. A. Structure-based design, synthesis, and biological evaluation of irreversible human rhinovirus 3C protease inhibitors. 8. pharmacological optimization of orally bioavailable 2-pyridone containing peptidomimetics. *J. Med. Chem.* **2003**, *46*, 4572−4585.
(41) Laszlo, P. *Organic Reactions: Simplicity and Logic*; Wiley-VCH: New York, NY, 1995.
(42) Slobbe, P.; Ruijter, E.; Orru, R. V. A. Recent applications of multicomponent reactions in medicinal chemistry. *Med. Chem. Commun.* **2012**, *3*, 1189−1218.
(43) Gopalakrishna, S. M.; Murugendrappa, M. V. Optical band gap determination of calcium doped lanthanum manganite nano particle tailored with polypyrrole. *AIP Conf. Proc.* **2018**, *1964*, No. 020012.
(44) Yoder, M. N. Wide bandgap semiconductor materials and devices. *IEEE Trans. Electron Devices* **1996**, *43*, 1633−1636.
(45) Chow, T. P. In *Wide Bandgap Semiconductor Power Devices for Energy Efficient Systems*, Proceedings of the IEEE Workshop Wide Bandgap Power Devices and Applications (WiPDA), IEEE 3rd Workshop, 2015; pp 402−405.
(46) Armstrong, K. O.; Das, S.; Cresko, J. In *Wide Bandgap Semiconductor Opportunities in Power Electronics*, Proceedings of the IEEE Workshop Wide Bandgap Power Devices and Applications (WiPDA), IEEE 4th Workshop, 2016; pp 259−264.
(47) Flicker, J.; Kaplar, R. In *Design Optimization of GaN Vertical Power Diodes and Comparison to Si and SiC*, Proceedings of the IEEE Workshop Wide Bandgap Power Devices and Applications (WiPDA), IEEE 5th Workshop, 2017; pp 31−38.
(48) Palmour, J. W.; Sheppard, S. T.; Smith, R. P.; Allen, S. T.; Pribble, W. L.; Smith, T. J.; Ring, Z.; Sumakeris, J. J.; Saxler, A. W.; Milligan, J. W. In *Wide Bandgap Semiconductor Devices and MMICs for RF Power Applications*, Electron Devices Meeting IEDM'01. Technical Digest, 2001; pp 17.4.1−17.4.4.
(49) Taniyasu, Y.; Kasu, M.; Makimoto, T. An aluminium nitride light-emitting diode with a wavelength of 210 nanometres. *Nature* **2006**, *441*, 325−328.
(50) Qiu, J.; Cheng, H.; DePuydt, J. M.; Haase, M. A. Recent developments in the MBE growth of wide bandgap II−VI semiconductors for laser diodes and LEDs. *J. Cryst. Growth* **1993**, *127*, 279−286.
(51) Manna, P.; Seth, S. K.; Bauzá, A.; Mitra, M.; Ray Choudhury, S.; Frontera, A.; Mukhopadhyay, S. pH dependent formation of unprecedented water−bromide cluster in the bromide salts of PTP assisted by anion−π interactions: synthesis, structure, and DFT Study. *Cryst. Growth Des.* **2014**, *14*, 747−755.
(52) Manna, P.; Seth, S. K.; Das, A.; Hemming, J.; Prendergast, R.; Helliwell, M.; Choudhury, S. R.; Frontera, A.; Mukhopadhyay, S. Anion induced formation of supramolecular associations involving lone pair−π and anion−π interactions in Co(II) malonate complexes: experimental observations, Hirshfeld surface analyses and DFT studies. *Inorg. Chem.* **2012**, *51*, 3557−3571.
(53) Mitra, M.; Manna, P.; Bauzá, A.; Ballester, P.; Seth, S. K.; Choudhury, S. R.; Frontera, A.; Mukhopadhyay, S. 3-Picoline Mediated Self-Assembly of M(II)−Malonate Complexes (M= Ni/Co/Mn/Mg/Zn/Cu) Assisted by Various Weak Forces Involving Lone Pair−π, $\pi-\pi$, and Anion$\cdots\pi$−Hole Interactions. *J. Phys. Chem. B* **2014**, *118*, 14713−14726.
(54) Seth, S. K.; Saha, I.; Estarellas, C.; Frontera, A.; Kar, T.; Mukhopadhyay, S. Supramolecular self-assembly of M-IDA complexes involving lone-pair$\cdots\pi$ interactions: crystal structures, hirshfeld surface analysis, and DFT calculations [H_2IDA= iminodiacetic acid, M= Cu (II), Ni (II)]. *Cryst. Growth Des.* **2011**, *11*, 3250−3265.
(55) Dey, A.; Middya, S.; Jana, R.; Das, M.; Datta, J.; Layek, A.; Ray, P. P. Light Induced Charge Transport Property Analysis of

DOI: 10.1021/acsomega.9b00289
ACS Omega 2019, 4, 7200−7212

Nanostructured Zns Based Schottky Diode. *J. Mater. Sci.: Mater. Electron.* **2016**, *27*, 6325−6335.
(56) Rhoderick, E. H. *Metal Semiconductors Contacts*; Oxford University Press: Oxford, 1978.
(57) Cheung, S. K.; Cheung, N. W. Extraction of Schottky diode parameters from forward current-voltage characteristics. *Appl. Phys. Lett.* **1986**, *49*, 85−87.
(58) Dey, A.; Layek, A.; Roychowdhury, A.; Das, M.; Datta, J.; Middya, S.; Das, D.; Ray, P. P. Investigation of Charge Transport Properties in Less Defective Nanostructured ZnO Based Schottky Diode. *RSC Adv.* **2015**, *5*, 36560−36567.
(59) Gupta, R. K.; Yakuphanoglu, F. Photoconductive Schottky diode based on Al/*p*-Si/SnS_2/Ag for optical sensor applications. *Sol. Energy* **2012**, *86*, 1539−1545.
(60) Miao, X.; Tongay, S.; Petterson, M. K.; Berke, K.; Rinzler, A. G.; Appleton, B. R.; Hebard, A. F. High Efficiency Graphene Solar Cells by Chemical Doping. *Nano Lett.* **2012**, *12*, 2745−2750.
(61) Blom, P. W. M.; de Jong, M. J. M.; van Munster, M. G. Electric-field and temperature dependence of the hole mobility in poly(p-phenylenevinylene). *Phys. Rev. B* **1997**, *55*, R656−R659.
(62) Perdew, J. P.; Levy, M. Physical Content of the Exact Kohn-Sham Orbital Energies: Band Gaps and Derivative Discontinuities. *Phys. Rev. Lett.* **1983**, *51*, No. 1884.
(63) Levine, Z. H.; Allan, D. C. Linear optical response in silicon and germanium including self-energy effects. *Phys. Rev. Lett.* **1989**, *63*, No. 1719.
(64) Hernández-Haro, N.; Ortega-Castro, J.; Martynov, Y. B.; Nazmitdinov, R. G.; Frontera, A. DFT prediction of band gap in organic-inorganic metal halide perovskites: An exchange-correlation functional benchmark study. *Chem. Phys.* **2019**, *516*, 225−231.
(65) Zhao, T.; Shi, W.; Xi, J.; Wang, D.; Shuai, Z. Intrinsic and Extrinsic Charge Transport in $CH_3NH_3PbI_3$ perovskites predicted from first-principles. *Sci. Rep.* **2016**, *6*, No. 19968.
(66) Mandal, T.; Dey, A.; Pathak, S.; Islam, M. M.; Konar, S.; Ortega-Castro, J.; Seth, S. K.; Ray, P.; Frontera, A.; Mukhopadhyaya, S. Structures, photoresponse properties and DNA binding abilities of 4-(4-pyridinyl)-2-pyridone salts. *RSC Adv.* **2019**, *9*, 9663−9677.
(67) Masum, A. A.; Chakraborty, M.; Pandya, P.; Halder, U. C.; Islam, M. M.; Mukhopadhyay, S. Thermodynamic study of rhodamine 123-calf thymus DNA interaction: determination of calorimetric enthalpy by optical melting study. *J. Phys. Chem. B* **2014**, *118*, 13151−13161.
(68) Islam, M. M.; Chakraborty, M.; Pandya, P.; Masum, A. A.; Gupta, N.; Mukhopadhyay, S. Binding of DNA with Rhodamine B: Spectroscopic and molecular modeling studies. *Dyes Pigm.* **2013**, *99*, 412−422.
(69) Pathak, S.; Kundu, A.; Pramanik, A. Regioselective synthesis of two types of highly substituted 2-pyridones through similar multicomponent reactions. *Tetrahedron Lett.* **2012**, *53*, 3030−3034.

DOI: 10.1021/acsomega.9b00289
ACS Omega 2019, 4, 7200−7212